Robotica: (2021) volume 39, pp. 2131–2152. © The Author(s), 2021. Published by Cambridge University Press.
doi:10.1017/S0263574721000229

Stable Calibrations of Six-DOF Serial Robots by Using Identification Models with Equalized Singular Values

Zhouxiang Jiang†‡* and Min Huang†

†*Institute of Electromechanical Engineering, Beijing Information Science & Technology University, 12 Xiaoying East Road, Qinghe, Haidian District, Beijing 100192, China*
E-mail: huangmin@bistu.edu.cn
‡ *Key Laboratory of Modern Measurement & Control Technology, Ministry of Education, Beijing Information Science & Technology University, Beijing, China*

(Accepted February 2, 2021. First published online: March 15, 2021)

SUMMARY
In typical calibration methods (kinematic or non-kinematic) for serial industrial robot, though measurement instruments with high resolutions are adopted, measurement configurations are optimized, and redundant parameters are eliminated from identification model, calibration accuracy is still limited under measurement noise. This might be because huge gaps still exist among the singular values of typical identification Jacobians, thereby causing the identification models ill conditioned. This paper addresses such problem by using new identification models established in two steps. First, the typical models are divided into the submodels with truncated singular values. In this way, the unknown parameters corresponding to the abnormal singular values are removed, thereby reducing the condition numbers of the new submodels. However, these models might still be ill conditioned. Therefore, the second step is to further centralize the singular values of each submodel by using a matrix balance method. Afterward, all submodels are well conditioned and obtain much higher observability indices compared with those of typical models. Simulation results indicate that significant improvements in the stability of identification results and the identifiability of unknown parameters are acquired by using the new identification submodels. Experimental results indicate that the proposed calibration method increases the identification accuracy without incurring additional hardware setup costs to the typical calibration method.

KEYWORDS: Industrial robot; Kinematic calibration; Non-kinematic calibration; Truncated singular values; Matrix balance

1. Introduction

1.1. Related literature

The absolute positioning accuracy of the end effector of an industrial robot depends on various factors. Among these factors, the most important is the geometric error,[1,2] which mainly results from the inaccurate manufacturing, misassembly, and the mechanical transmission error.[3] The joint flexibility that results in non-negligible elastic deformation under the external payload or self-gravity of robots also plays an important role in determining positioning accuracy.[1,4,5]

Given the small values of the geometric error and compliance parameter, high-resolution devices play an indispensablerole for their identifiability. The most widely used of these devices include

* Corresponding author. E-mail: jiangzhouxiang@bistu.edu.cn

https://doi.org/10.1017/S0263574721000229 Published online by Cambridge University Press

the Faro or Leica laser trackers given their high measurement accuracy.[3,6–10] Another optical instrument called C-track 780 CMM, which has a measurement accuracy of 0.03 mm, has also attracted wide usage.[11] In addition to noncontact optical methods, the Renishaw QC20-W telescoping ballbar (usually for calibrating machine tools) with 3–7 μm length measurement accuracy has been used.[12] Another contact measuring device called the touch-trigger probe (commonly for workpiece inspection) has also been used.[13,14] This device has also been combined with the FARO arm, which has a positioning accuracy of 0.018 mm, to calibrate the robot base frame.[15] Camera with high resolution has also been adopted.[16]

Although these devices can provide high resolutions by using the available technology, the small positioning errors of the end effector might still be covered by inevitable measurement noise at improperly selected measurement configurations.[17–19] To address this problem, most of the studies have optimized their measurement configurations before the calibration. In this way, the observability index[17–19] of the identification model can be significantly improved, that is, the effect of unknown parameters on the positioning error of the end effector is maximized, thereby reducing the influence of unwanted noise. To further improve the calibration accuracy, Bayesian inference methods[20] and iterative Levenberg-Marquardt algorithm[21] have also been adopted in the stage of parameters identification. And the POE model has also been improved to minimize the influence of measurement noise on the evaluation of orientation errors of end effector.[22]

However, some studies show that despite the measurement configurations are optimized, various identification algorithms are adopted, and some typical identification models are improved, the identifiability of unknowns and the stability of results still need to be improved. Klimchik et al.[23] proposed a reduction method that practically eliminates nonidentifiable compliance parameters from the identification model. In this way, the rest unknowns become practically identifiable and produce highly accurate results. Kamali et al.[24] designed a cable-driven moving platform that applies a wrench with different directions on the end effector of a robot to further increase the observability index of the non-kinematic identification model. Similarly, Theissen et al.[25] designed a measurement method that uses a loaded double ball bar to customize the applied wrench vectors. Huang et al.[26] found that ill conditioning may still emerge from multicollinearity even though the identification Jacobian is full rank. Accordingly, they proposed a two-step procedure involving coarse and fine calibrations to stabilize the identification model amidst the presence of measurement uncertainty.

1.2. Motivations

1.2.1. For serial robot, only the identifiability of compliance parameter is considered. Most efforts have focused on the identifiability of compliance parameters, whereas those of geometric errors have been rarely considered (the multicollinearity problem emerging in kinematic calibration[26] has only been addressed for hybrid polishing robots but not for widely used serial robots). However, geometric errors contain various elements with different weights in the identification model, which may lead to ill-conditioned Jacobians with fluctuated singular values.

1.2.2. Expensive additional instruments are necessary for the improvement of compliance parameters' identifiability. For instance, given the necessity of expensive instruments added for laser tracker, the mechanisms proposed by Kamali et al.[24] and Theissen et al.[25] may be unavailable for ordinary users despite their effectiveness.

1.3. Contribution of this work

1.3.1. Considers the identifiability of unknown parameters both in the kinematic and non-kinematic calibrations. The singular values of these two typical identification models are analyzed. The unknown parameters corresponding to abnormally low singular values are removed from identification models and separately identified by using a non-model-based method. New identification submodels with better observability indices and condition numbers are established for the remaining unknowns with higher singular values. Then, these submodels with truncated singular values are further stabilized by using a matrix balanced method that equalizes singular values into smaller ranges. In this way, the identifiability of unknowns and stability of models can both be significantly improved.

https://doi.org/10.1017/S0263574721000229 Published online by Cambridge University Press

Table I. Nominal kinematic parameters and range of the six-DOF robot.

Joint	**α(rad)**	**a(mm)**	**θ(rad)**	**d(mm)**	**β (rad)**
1	0	0	$\theta_1[-17\pi/36, 17\pi/36]$	400	–
2	$-\pi/2$	170	$\theta_2-\pi/2[-\pi/4, 2\pi/3]$	0	–
3	0	650	$\theta_3[-17\pi/72, 13\pi/36]$	–	0
4	$-\pi/2$	155.7	$\theta_4[-\pi/2, \pi/2]$	605.4	–
5	$\pi/2$	0	$\theta_5[-\pi/3, \pi/3]$	0	–
6	$-\pi/2$	0	$\theta_6[-\pi/2, \pi/2]$	147.5	–

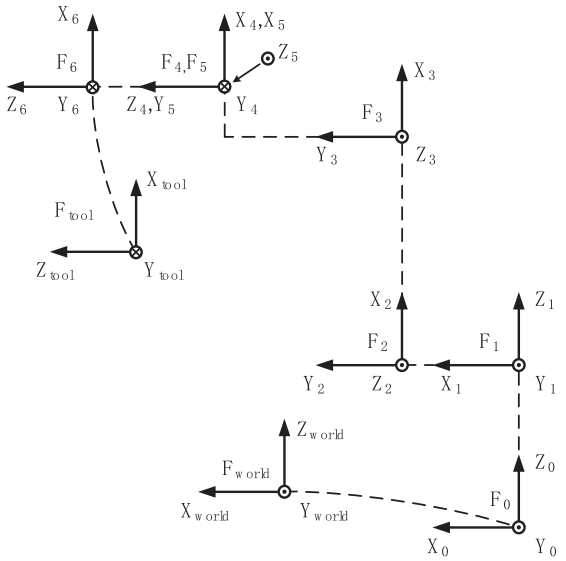


Fig. 1. Frame assignment of the six-DOF industrial robot.

1.3.2. Implements the new calibration method by using the same experimental setup with that of typical calibration methods. No additional expensive mechanisms are employed because the new identification submodels and new measurement configurations are all generated by only using the software method without additional hardware costs.

The remainder of this article is organized as follows. Section 2 presents two typical identification models for kinematic and non-kinematic calibrations. Section 3 analyzes the singular values of these models. Section 4 proposes a two-step method for establishing identification models with equalized singular values. Section 5 compares the effectiveness of the typical and proposed methods by performing a set of simulations. Section 6 further verifies such effectiveness by performing a real calibration. Section 7 concludes the paper and presents directions for further work.

2. Typical Identification Models

Here, two typical identification models are briefly introduced. The first model only considers the geometric errors[9] and the second is used for a non-kinematic calibration that takes the geometric errors and compliance parameters into account.[10] The prior knowledge for these calibration methods is the frame assignment shown in Fig. 1 and the nominal kinematic parameters are given in Table I.

The typical models for kinematic and non-kinematic calibration are both established based on homogeneous transformation matrices[1] which denote the pose of frame F_i with respect to $F_{i_{-1}}$ by using

$$H_i^{i-1} = Trans_z(d_i)Rot_z(\theta_i)Trans_x(a_i)Rot_x(\alpha_i). \quad (1)$$

https://doi.org/10.1017/S0263574721000229 Published online by Cambridge University Press

The DH (Denavit-Hartenberg) parameter[1] d_3 is substituted by the MDH (Modified Denavit-Hartenberg) parameter[1] β_3 to decouple d_2 and d_3. Accordingly, the pose of F_3 with respect to F_2 is calculated as

$$H_i^{i-1} = Rot_z(\theta_i)Trans_x(a_i)Rot_x(\alpha_i)Rot_y(\beta_i). \tag{2}$$

If the base frame F_0, world frame F_{world} and end-effector frame F_{tool} are established and rotation angles are denoted by using $q = [\theta_1, \theta_2, \ldots, \theta_6]^T$, then the transformation from F_{world} to F_{tool} is

$$H(q) = H_0^{world}H_1^0H_2^1H_3^2H_4^3H_5^4H_6^5H_{tool}^6. \tag{3}$$

2.1. The typical model for kinematic calibration

To establish the mapping from the geometric errors of six joints to the pose errors of the end effector, a 24×1 vector Δu_K is formed as

$$\Delta u_K = [\delta\alpha_1, \delta a_1, \delta\theta_1, \delta d_1, ..., \delta\alpha_6, \delta a_6, \delta\theta_6, \delta d_6]^T \tag{4}$$

The corresponding identification Jacobian J_K with a dimension of 6×24 at the l_Kth measurement configuration (where $l_K = 1, 2, \ldots, m_K$ denotes the order of measurement configurations for kinematic calibration) is established as

$$J_{K(l_K)} = [J_{\alpha_1}, J_{a_1}, J_{\theta_1}, J_{d_1}, ..., J_{\alpha_6}, J_{a_6}, J_{\theta_6}, J_{d_6}]_{(l_K)}, \tag{5}$$

where $J_{\alpha 1}, J_{a1}, \ldots, J_{\theta 6}, J_{d6}$ are 6×1 Jacobians[9] that represent the mapping from the corresponding kinematic error to the caused pose errors of the end effector. Their elements are obtained by using the differential transformation theory[1] and

$$\begin{bmatrix} n_x & o_x & a_x & p_x \\ n_y & o_y & a_y & p_y \\ n_z & o_z & a_z & p_z \\ 0 & 0 & 0 & 1 \end{bmatrix} = H_{i+1}^i H_{i+2}^{i+1} \ldots H_6^5 H_{tool}^6 \tag{6}$$

which is acquired from Eqs. (1)–(3). The transformation from frame F_6 to F_{tool} is achieved during real calibration.[6] Then the Jacobian J_K (with a dimension of $6m_K$×24) for m measurement configurations is obtained and the kinematic model can be given as

$$\Delta E_K = J_K \Delta u_K, \tag{7}$$

where ΔE_K (also with the dimension of $6m_K$×24) is the pose error vector of the end effector. The corresponding kinematic identification model[10] is

$$\Delta u_K = J_K^+ \Delta E_K, \tag{8}$$

where the superscript '+' represents the pseudo-inverse matrix.

2.2. The typical model for non-kinematic calibration

In addition to the abovementioned geometric errors, joint flexibility also plays an important role.[4,6,7,10,13,19,20] If a more complete and accurate calibration is necessary, then the compliance parameters $\{\lambda_2, \lambda_3, \lambda_4, \lambda_5\}$ of joints 2–5 (dependent on external payload)and the compliance parameters $\{\xi_1, \xi_2, \xi_3\}$ (dependent on the gravities of links 2–3) cannot be ignored (details are given in ref. [10]). Two error vectors are used to lump these compliance parameters as $\Delta u_E = [\lambda_2, \lambda_3, \lambda_4, \lambda_5]^T$ and $\Delta u_G = [\xi_1, \xi_2, \xi_3]^T$,[10] respectively. The mappings from Δu_E and Δu_G to the caused end effector pose errors ΔE_E and ΔE_G are established as

$$\Delta E_E = J_E \Delta u_E \tag{9}$$

and

$$\Delta E_G = J_G \Delta u_G, \tag{10}$$

https://doi.org/10.1017/S0263574721000229 Published online by Cambridge University Press

respectively. The Jacobians J_E and J_G (elaborated in Chen et al.[10]) are established respectively by using the Jacobians $J_{E(lc)}$ and $J_{G(lc)}$ (at l_Cth measurement configuration, where $l_C = 1, 2, \ldots, m_C$ denotes the order of measurement configurations for non-kinematic calibration) given as

$$\begin{cases} J_{E(l_C)} = J^{2,3,4,5}_{K_\theta(l_C)} diag[J^{2,3,4,5}_{F(l_C)} Ad_{(l_C)}(H^{tool}_e)^e F_e] \\ J_{G(l_C)} = J^{2,3}_{K_\theta(l_C)} C_{G(l_C)} \end{cases}, \tag{11}$$

where the kinematic and force Jacobians are established as

$$\begin{cases} J^{2,3,4,5}_{K_\theta(l_C)} = [J_{\theta_2}, J_{\theta_3}, J_{\theta_4}, J_{\theta_5}]_{(l_C)} \\ J^{2,3}_{K_\theta(l_C)} = [J_{\theta_2}, J_{\theta_3}]_{(l_C)} \\ J^{2,3,4,5}_{F(l_C)} = [J^{2,3,4,5}_{K_\theta(l_C)}]^T \end{cases} \tag{12}$$

Definitions of $J_{\theta 2}$, $J_{\theta 3}$, $J_{\theta 4}$, $J_{\theta 5}$ are the same with those in Eq. (5). And the force adjoint matrix $Ad_{(lc)}(\cdot)$ at l_Cth measurement configuration is

$$Ad_{(l_C)}(H^{tool}_e) = \begin{bmatrix} {}^{tool}_{e}R & 0 \\ [{}^{tool}_{e}p]{}^{tool}_{e}R & {}^{tool}_{e}R \end{bmatrix}, \tag{13}$$

where

$$H^{tool}_e = [(H^6_e)^{-1} H^6_{tool}]^{-1} \begin{bmatrix} {}^{tool}_{e}R & {}^{tool}_{e}p \\ 0 & 1 \end{bmatrix} \tag{14}$$

represents the transformation from frame F_{tool} to the external payload frame F_e, and

$$[{}^{tool}_{e}p] = \begin{bmatrix} 0 & -{}^{tool}_{e}p_z & {}^{tool}_{e}p_y \\ {}^{tool}_{e}p_z & 0 & -{}^{tool}_{e}p_x \\ -{}^{tool}_{e}p_y & {}^{tool}_{e}p_x & 0 \end{bmatrix}. \tag{15}$$

In Eq. (11), ${}^eF_e = [0, 0, -m_e g, 0, 0, 0]^T$ is the external payload vector,[10] where m_e is the mass of the external payload and $g = 9.8$ m/s.[2] In Eq. (11), the coefficient matrix $C_{G(lc)}$ is

$$C_{G(l_C)} = \begin{bmatrix} \sin\theta_2 & \cos(\theta_2 + \theta_3) & 0 \\ 0 & 0 & \cos(\theta_2 + \theta_3) \end{bmatrix}. \tag{16}$$

Then, if the following combinations

$$\begin{cases} \Delta u_C = [\Delta u_K^T, \Delta u_E^T, \Delta u_G^T]^T \\ J_C = [J_K, J_E, J_G] \\ \Delta E_C = \Delta E_K + \Delta E_E + \Delta E_G \end{cases} \tag{17}$$

are used, then the non-kinematic model is established as

$$\Delta E_C = J_C \Delta u_C. \tag{18}$$

The corresponding non-kinematic identification model[10] is

$$\Delta u_C = J_C^+ \Delta E_C. \tag{19}$$

3. Problems of the Typical Identification Models

The stability of the identification models in Eqs. (8) and (19) can be evaluated according to the condition numbers[27] of Jacobians J_K and J_C. The simulation is performed on MATLAB. In Sections 3.1 and 3.2, the measurement configurations for simulations are optimized by using the DETMAX algorithm,[28] and the numbers are acquired as $m_K = 20$ and $m_C = 26$. Then, according to Sections 2.1

https://doi.org/10.1017/S0263574721000229 Published online by Cambridge University Press

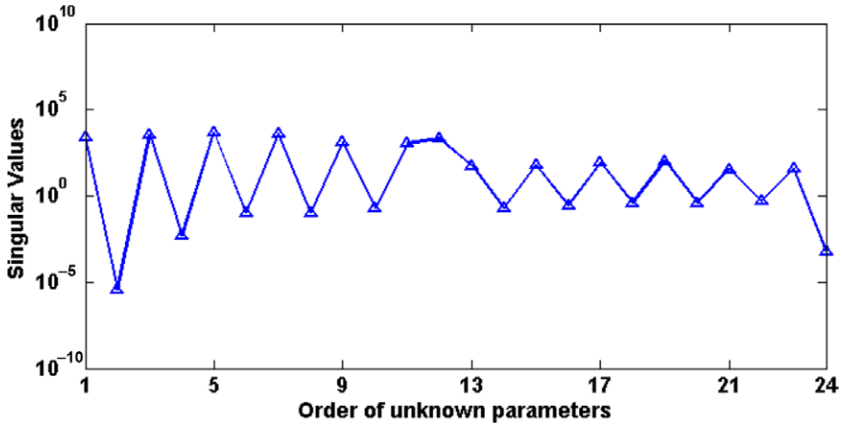


Fig. 2. Singular values of typical identification model for kinematic calibration.

and 2.2, Jacobians J_K and J_C can be established. The condition number is calculated by using $cond = \sigma_{max}/\sigma_{min}$, where σ_{max} and σ_{min} are the maximum and minimum singular values, respectively, of J_K or J_C.[27] The singular values are acquired by using the singular value decomposition (SVD).[17]

3.1. Problems of typical identification models for kinematic calibration

The result of condition number is $cond(J_K) = 1.2\times10^9$. According to ref. [27], if the change of measuring pose errors (due to measurement noise) is denoted by $\delta\Delta E_K$ and the caused change of identification results is denoted by $\delta\Delta u_K$, it is acquired that

$$\frac{\|\delta\Delta u_K\|}{\|\Delta u_K\|} \le cond(J_K)\frac{\|\delta\Delta E_K\|}{\|\Delta E_K\|}. \tag{20}$$

If a Faro vantage laser tracker is adopted, it can be roughly assumed that $\|\delta\Delta E_K/\Delta E_K\| = 0.02$ according to the specifications of instrument. Therefore, it is acquired that $\|\delta\Delta u_K/\Delta u_K\| = cond(J_K)\times\|\delta\Delta E_K/\Delta E_K\| = 2.4\times10^7$, which means the maximum change $\delta\Delta u_K$ of identification results under the measurement noise might be 2.4×10^7 times larger than their real values Δu_K. Although this is only a possibility rather than a certainty, the identification results might be probably unconvincing if the measurement noise is not well controlled. According to the definition $cond = \sigma_{max}/\sigma_{min}$ and Eq. (20), $cond(J_K) = 1$ is preferred.[27] Therefore, it is necessary to reduce $cond(J_K)$. Given that the column vectors of Jacobian J_K are all independent (i.e. there is no collinearity among the unknown parameters to be identified), the ill conditioning of J_K is not attributed to parameter redundancy but some of the parameters themselves. In other words, some abnormal singular values σ might enlarge the gaps between $\sigma_{\max}$ and $\sigma_{\min}$.

Accordingly, a simulation is used to observe the singular values of Jacobian J_K. The sum of elements' absolute values (1-norm) of each column could be used to represent the weight of each column in J_K, that is, the weight of each unknown parameter in Δu_K. The singular values could also be used to represent the weights of columns in J_K (weights of unknown parameters in Δu_K) but arrange them in a descending order in the diagonal matrix SofSVD ($J_K = USV$). Therefore, the one-to-one correspondence between unknown parameter and singular value can be acquired by rearranging the singular values of J_K in the same order with that of the unknown parameters in Δu_K (from 1 to 24) instead of the descending order in SVD. Specifically, the first step is calculating the 1-norm of each column of J_K. The second step is rearranging these columns (as well as the corresponding unknown parameters in Δu_K) according to the descending order of their 1-norm values. Now, the first unknown parameter in the rearranged Δu_K corresponds to the first (maximum) singular value in matrix S, the second corresponds to the second, and so on. The last unknown parameter in the rearranged Δu_K corresponds to the last (minimum) singular value in matrix S. Finally, the last step is rearranging the singular values (corresponding to certain unknown parameters) according to the original order of unknown parameters in Δu_K. As shown in Fig. 2, the first singular value corresponds to the first unknown parameter $\delta\alpha_1$(with the order number '1') in vector Δu_K, whereas the last singular value

https://doi.org/10.1017/S0263574721000229 Published online by Cambridge University Press

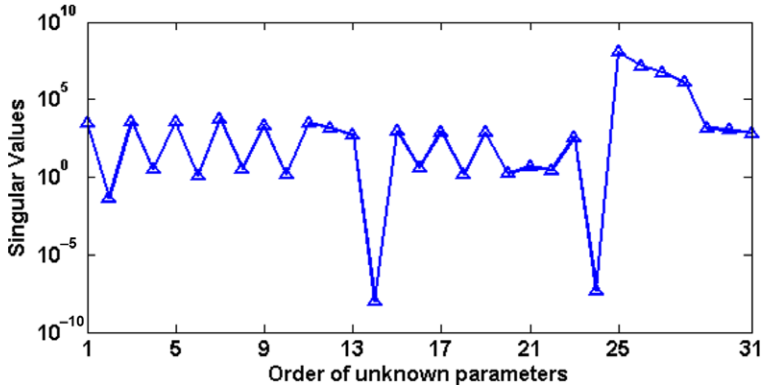


Fig. 3. Singular values of typical identification model for non-kinematic calibration.

corresponds to the last unknown parameter δd_6 (with the order number '24'). Now, it is convenient to pick out the unknown parameters that correspond to abnormal singular values.

As shown in Fig. 2, the singular values corresponding to the rotational geometric errors (with order numbers '1', '3', '5', '7', '9', '11', '12', '13', '15', '17', '19', '21', and '23') of J_K are centralized within a small range, whereas those corresponding to the translational geometric errors (with order numbers '2', '4', '6', '8', '10', '14', '16', '18', '20', '22', and '24') break this stability. Besides, it is seen that the rotational geometric errors of joints 1–3 (with order numbers '1', '3', '5', '7', '9', '11', '12', and '13') have higher singular values than those of joints 4–6 (with order numbers '15', '17', '19', '21', and '23') do.

3.2. Problems of typical identification models for non-kinematic calibration

The result of condition number is $cond(J_C) = 1.0\times10^{16}$. According to Section 3.1, the value of $cond(J_C)$ is also too large for convincing identification results. Therefore, it is also necessary to reduce $cond(J_K)$ as much as possible.

Like Section 3.1, a simulation is also used to observe the singular values of Jacobian J_C. They are rearranged in the order of the unknown parameters in Δu_C (from 1 to 31). Specifically, the first singular value corresponds to the first unknown parameter $\delta\alpha_1$ in Δu_C with the order number '1', whereas the last singular value corresponds to the last unknown parameter ξ_3 with the order number '31'.

Compared with Fig. 2, Fig. 3 shows the singular values corresponding to the compliance parameters (Δu_E and Δu_G) additionally. The results indicate that Δu_E (with order numbers '25' – '28') have higher singular values than other parameters do, while the singular values of Δu_G (with order numbers '29' – '31') are similar with those of rotational geometric (with order numbers '1', '3', '5', '7', '9', '11', '12', '13', '15', '17', '19', '21', and '23'). Similar with the results in Fig. 2, the translational geometric errors (with order numbers '2', '4', '6', '8', '10', '14', '16', '18', '20', '22', and '24') still have much lower singular values than rotational geometrics do. Also, rotational geometric error $\delta\alpha_6$ (with order number '21') has lower singular value than those of other rotational ones do.

4. Identification Models with Equalized Singular Values

4.1. Submodels with truncated singular values

4.1.1. Kinematic submodels with truncated singular values. According to the analysis in Section 3.1, the unknown parameters with abnormal singular values (weights) should be separately identified. Therefore, the error vector Δu_K in Eq. (4) is divided into three parts as

$$\begin{cases} \Delta u_K^{(1)} = [\delta\alpha_1, \delta\theta_1, \delta\alpha_2, \delta\theta_2, \delta\alpha_3, \delta\theta_3, \delta\beta_3]^T \\ \Delta u_K^{(2)} = [\delta\alpha_4, \delta\theta_4, \delta\alpha_5, \delta\theta_5, \delta\alpha_6, \delta\theta_6]^T \\ \Delta u_K^{(3)} = [\delta a_1, \delta d_1, ..., \delta a_6, \delta d_6]^T \end{cases} . \tag{21}$$

https://doi.org/10.1017/S0263574721000229 Published online by Cambridge University Press

The translational geometric errors (vectors with superscript '(3)') should be identified by using the CPA method,[29–31] whereas the rotational errors (vectors with superscripts '(1)' and '(2)') should be identified by using the reduced models. Correspondingly, the Jacobian $J_{K(lk)}$in Eq. (5) is divided into

$$\begin{cases} J^{(1)}_{K(l_{K1})} = [J_{\alpha_1}, J_{\theta_1}, J_{\alpha_2}, J_{\theta_2}, J_{\alpha_3}, J_{\theta_3}, J_{\beta_3}]_{(l_{K1})} \\ J^{(2)}_{K(l_{K2})} = [J_{\alpha_4}, J_{\theta_4}, J_{\alpha_5}, J_{\theta_5}, J_{\alpha_6}, J_{\theta_6}]_{(l_{K2})} \end{cases}, \tag{22}$$

where $l_{K1} = 1, 2, \ldots, m_{K1}$ and $l_{K2} = 1, 2, \ldots, m_{K2}$ denote the order of measurement configurations for joints 1–3 and 4–6, respectively. And definitions of $J_{\alpha 1}, J_{\theta 1}, \ldots, J_{\alpha 6}, J_{\theta 6}$ are the same with those in Eq. (5). Then, the kinematic model in Eq. (7) for geometric errors can be divided into

$$\begin{cases} \Delta E^{(1)}_K = J^{(1)}_K \Delta u^{(1)}_K \\ \Delta E^{(2)}_K = J^{(2)}_K \Delta u^{(2)}_K \end{cases}, \tag{23}$$

where each Jacobian has truncated singular values with a similar magnitude (i.e. reduced condition numbers). Accordingly, with the improved stability of the submodels, more accurate identification results of Δu_K can be obtained.

4.1.2. Non-kinematic submodels with truncated singular values. According to the analysis in Section 3.2, the unknown parameters with abnormal singular values (weights) should be separately identified. However, Δu_E which have higher singular values are difficult to be identified separately (installation of sensors on the end effector should be considered as a part of external payload which is nonignorable). Therefore, the error vector Δu_C in Eq. (17) is also divided into three parts as

$$\begin{cases} \Delta u^{(1)}_C = [(\Delta u^{(1)}_K)^T, \lambda_2, \lambda_3, \Delta u^T_G]^T \\ \Delta u^{(2)}_C = [(\Delta u^{(2)}_K)^T, \lambda_4, \lambda_5]^T \\ \Delta u^{(3)}_C = \Delta u^{(3)}_K = [\delta a_1, \delta d_1, ..., \delta a_6, \delta d_6]^T \end{cases}. \tag{24}$$

Correspondingly, the Jacobian $J_{E(lc)}$ in Eq. (11) is divided as

$$\begin{cases} J^{(1)}_{E(l_{C1})} = J^{2,3}_{K_\theta(l_{C1})} diag[J^{2,3}_{F(l_{C1})} Ad_{(l_{C1})}(H^{tool}_e)^e F_e] \\ J^{(2)}_{E(l_{C2})} = J^{4,5}_{K_\theta(l_{C2})} diag[J^{4,5}_{F(l_{C2})} Ad_{(l_{C2})}(H^{tool}_e)^e F_e] \end{cases}, \tag{25}$$

where the kinematic and force Jacobians are established as

$$\begin{cases} J^{2,3}_{K_\theta(l_{C1})} = [J_{\theta_2}, J_{\theta_3}]_{(l_{C1})} \\ J^{4,5}_{K_\theta(l_{C2})} = [J_{\theta_4}, J_{\theta_5}]_{(l_{C2})} \\ J^{2,3}_{F(l_{C1})} = [J^{2,3}_{K_\theta(l_{C1})}]^T \\ J^{4,5}_{F(l_{C2})} = [J^{4,5}_{K_\theta(l_{C2})}]^T \end{cases}. \tag{26}$$

In Eq. (25), the force adjoint matrices $Ad_{(lc1)}(\cdot)$ and $Ad_{(lc2)}(\cdot)$ are established in the same way as Eq. (13). $l_1 = 1, 2, \ldots, m_{C1}$ and $l_2 = 1, 2, \ldots, m_{C2}$ denote the order of measurement configurations for joints 1–3 and 4–6, respectively. Definition of ${}^eF_e$ is the same with that in Eq. (11). Definitions of $J_{\theta 2}$–$J_{\theta 5}$ are the same with those in Eq. (5). According to the definitions of Jacobians J_G, J_K, and J_E in Eqs. (11), (22), and (25), respectively, the combined J_C in Eq. (17) is reduced and reconstructed as

$$\begin{cases} J^{(1)}_C = [J^{(1)}_K, J^{(1)}_E, J_G] \\ J^{(2)}_C = [J^{(2)}_K, J^{(2)}_E] \end{cases}. \tag{27}$$

https://doi.org/10.1017/S0263574721000229 Published online by Cambridge University Press

Accordingly, the non-kinematic model in Eq. (18) is modified into

$$\begin{cases} \Delta E_C^{(1)} = J_C^{(1)} \Delta u_C^{(1)} \\ \Delta E_C^{(2)} = J_C^{(2)} \Delta u_C^{(2)} \end{cases}, \tag{28}$$

where each Jacobian has truncated singular values with a similar magnitude (i.e. reduced values of condition numbers). Accordingly, with the improved stability of the submodels, more accurate identification results of Δu_C can also be acquired.

4.2. Submodels with balanced identification Jacobians

Based on truncation, the singular values in each submodel (Eqs. (23) and (28)) can be further equalized by using a two-step matrix balance method. The first step is column balance. If B is a diagonal matrix used for the column balance, then an equivalence relation between two equations can be acquired as

$$\Delta E_*^{(\#)} = J_*^{(\#)} \Delta u_*^{(\#)} \Leftrightarrow \Delta E_*^{(\#)} = (J_*^{(\#)} B) B^{-1} \Delta u_*^{(\#)}, \tag{29}$$

where the superscript '(#)'corresponds to the superscripts '(1)' (joints 1–3) or '(2)' (joints 4–6), and the subscript '*' corresponds to the subscripts 'K' (kinematic) or 'C' (non-kinematic), respectively. Thus, the column balance method can be used for both Eqs. (23) and (28). Matrix B should be established with the following constraints

$$\begin{cases} rank(J_*^{(\#)} B) = rank(J_*^{(\#)}) \\ cond(J_*^{(\#)} B) < cond(J_*^{(\#)}) \\ observe(J_*^{(\#)} B) > observe(J_*^{(\#)}) \end{cases}, \tag{30}$$

where $rank(\cdot)$, $cond(\cdot)$, and $observe(\cdot)$ represent the rank, condition number, and observability index[6] of Jacobian '$\cdot$', respectively. Accordingly, the column balance criterion is determined by computing the maximum1-norm(denoted by $\|\cdot\|_1$) of columns as

$$J_{col_max} = max\left\{ \left\| Col(J_*^{(\#)}, 1) \right\|_1, \left\| Col(J_*^{(\#)}, 2) \right\|_1, ..., \left\| Col(J_*^{(\#)}, n) \right\|_1 \right\}, \tag{31}$$

where $Col(M,y)$ denotes the yth column of matrix M. Afterward, the column balance factor (i.e. the diagonal elements of matrix B) is calculated as

$$b_{col,col} = \frac{J_{col_max}}{\left\| Col(J_*^{(\#)}, col) \right\|_1}, \tag{32}$$

where $col = 1,2,\ldots,n$ and $n = rank(B)$. Equation (32) indicates that a column vector with lower weight is multiplied by a higher $b_{col,col}$. After that, the 1-norms of all columns in Jacobian JB are the same, that is, the weights of columns are equalized.

The second step is row balance. A diagonal matrix A is generated. After the left multiplication of A, an equivalence relation between two equations can be acquired as

$$A\Delta E_*^{(\#)} = A J_*^{(\#)} \Delta u_*^{(\#)} \Leftrightarrow A\Delta E_*^{(\#)} = A J_*^{(\#)} B B^{-1} \Delta u_*^{(\#)}, \tag{33}$$

where the denotations of superscript '(#)' and the subscript '*' are the same with those in Eq. (29). Thus, the row balance method can also be used for both Eqs. (23) and (28). The row balance matrix A should be constructed with the following constraints

$$\begin{cases} rank(A J_*^{(\#)} B) = rank(J_*^{(\#)} B) \\ cond(A J_*^{(\#)} B) < cond(J_*^{(\#)} B) \\ observe(A J_*^{(\#)} B) > observe(J_*^{(\#)} B) \end{cases}. \tag{34}$$

Accordingly, the maximum 1-norm can be determined by rows as

$$J_{row_max} = max\left\{ \left\| Row(J_*^{(\#)} B, 1) \right\|_1, \left\| Row(J_*^{(\#)} B, 2) \right\|_1, ..., \left\| Row(J_*^{(\#)} B, 6m) \right\|_1 \right\}, \tag{35}$$

https://doi.org/10.1017/S0263574721000229 Published online by Cambridge University Press

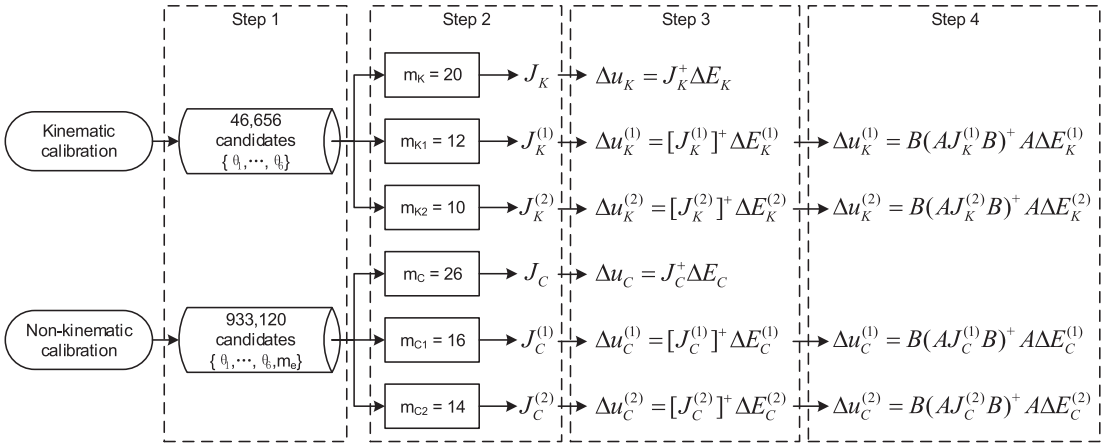


Fig. 4. Steps of simulation preparation.

where $Row(M,x)$ denotes the xth row of matrix M. The row balance factor (i.e. the diagonal elements of matrix A) is calculated as

$$a_{row,row} = \frac{J_{row_max}}{\left\| Row(J_*^{(\#)}B,\ row) \right\|_1}, \tag{36}$$

where $row = 1,2,\ldots,6m$, $6m = rank(A)$, and m represents the number of measurement configurations (m can be m_K, m_{K1}, m_{K2}, m_C, m_{C1} and m_{C2}). Equation (36) indicates that a row vector with lower weight is multiplied by a higher $a_{row,row}$. Therefore, the 1-norms of all rows in Jacobian AJB are the same, that is, the weights of rows are also equalized.

After these two steps, the identification submodels (Eqs. (23) and (28)) are established as

$$\Delta u_*^{(\#)} = B(AJ_*^{(\#)}B)^{+}A\Delta E_*^{(\#)}. \tag{37}$$

The balance matrices A and B differ for various denotations of '(#)' and '*'. In other words, each submodel in Eqs. (23) and (28) can be transformed into the form of Eq. (37) with corresponding denotations of '(#)' and '*' by using the matrix balance method. Given that more equalized singular values (smaller condition numbers) are available from the balanced Jacobian AJB than the reduced J (in Section 4.1), more accurate identification results of Δu can be acquired.

5. Simulation of Improved Identification Models

The simulation is performed on MATLAB. The analysis aims to compare the condition numbers, observability indices, singular values, stability of results, and calibration accuracy between the typical (in Sections 2) and improved identification models (in Sections 4.1 and 4.2).

5.1. Simulation preparation

The performances of Eqs. (8), (19), (23), (28) and their corresponding balanced forms in Eq. (37) are compared. The preparations are illustrated in Fig. 4. In step 1, for the kinematic calibrations, six rotation angles are taken on average in the motion range of each joint, thereby generating 6^6 = 46,656 candidate configurations. For non-kinematic calibrations, the optimization not only considers the best combinations of joint angles $\{\theta_1, \theta_2, \theta_3, \theta_4, \theta_5, \theta_6\}$ but also involves the selection of proper external payloads m_e (0, 2, 4, 6 and 8 kg are available). Therefore, 5×6^6 = 933,120 candidate configurations are generated. Then, step 2 selects optimal measurement configurations by using the DETMAX algorithm[28] to establish the Jacobians in Eqs. (7), (18), (23) and (28), respectively. This step acquires the number of measurement configurations for each Jacobian (m_K = 20, m_{K1} = 12, m_{K2} = 10, m_C = 26, m_{C1} = 16, m_{C2} = 14). Step 3 establishes identification model with truncated singular values corresponding to Eqs. (7), (18), (23) and (28). Step 4 establishes identification models with balanced Jacobians corresponding to Eqs. (23) and (28). These identification models will be used in Section 5.2.

https://doi.org/10.1017/S0263574721000229 Published online by Cambridge University Press

Table II. Condition numbers and observability indices of Jacobians in kinematic models.

Jacobians	J_K	$J_K^{(1)}$	$J_K^{(2)}$	$AJ_K^{(1)}B$	$AJ_K^{(2)}B$
Observability index	1.2	226.3	198.1	1433.2	685.6
Condition number	1.2×10^{9}	37.6	1.8	2.3	1.6

Table III. Condition numbers and observability indices of Jacobians in non-kinematic models.

Jacobians	J_C	$J_C^{(1)}$	$J_C^{(2)}$	$AJ_C^{(1)}B$	$AJ_C^{(2)}B$
Observability index	22.6	1264	1612	3.9×10^{7}	4.3×10^{6}
Condition number	1.0×10^{16}	1.2×10^{6}	2.2×10^{4}	77.6	1.8

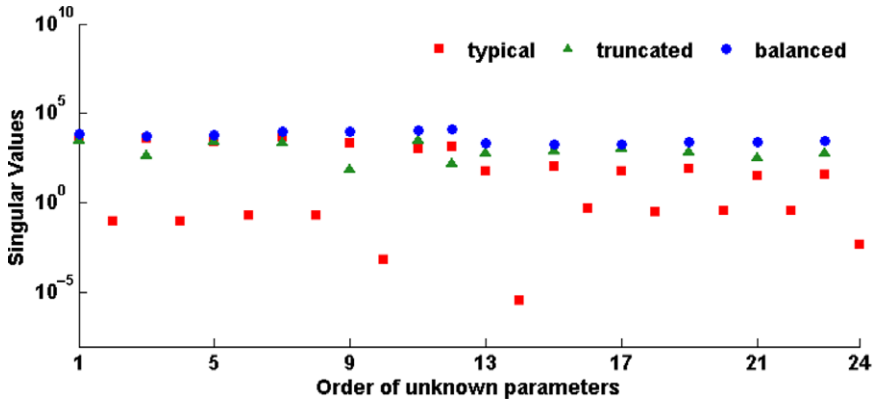


Fig. 5. Singular values of Jacobians in kinematic models.

5.2. Simulation and results

5.2.1. Condition number and observability index. The condition number and observability index[16–18] of the Jacobians in the abovementioned identification models are presented in Tables II and III. Results indicate that the condition numbers can be reduced by successively using submodels with truncated singular values (Section 4.1) and balanced identification Jacobians (Section 4.2). And the observability index O_1[17–19] can also be significantly improved in this way.

5.2.2. Singular values. To obtain additional details regarding the improvement of kinematic identification models, the singular values of Jacobians in Eqs. (8), (23), and (37) are compared in Fig. 5. The ranges of singular values are significantly narrowed down in the submodels with truncated singular values (Eq. (23)) by eliminating the abnormal singular values of translational geometric errors and by dividing the rotational geometric errors into two groups (Section 4.1). However, some unknowns ($\delta\alpha_1$ with the order number '1', $\delta\alpha_3$ with the order number '9' and $\delta\beta_3$ with the order number '12') still have relatively different singular values. Accordingly, the adopted matrix balance method (Section 4.2) pulls up all singular values to a similar magnitude, thereby resulting in highly equalized singular values.

For non-kinematic identification models, the singular values of Jacobians in Eqs. (19), (28) and (37) are compared in Fig. 6. Results indicate that the condition number and observability index of non-kinematic models are also significantly improved by truncating and balancing the singular values of Jacobians. By comparison, the matrix balance method (Section 4.2) is much more effective in non-kinematic models than in kinematic ones because it smoothes the abnormality of the singular values of compliance parameters (with the order numbers '26', '27', '28', and '29').

https://doi.org/10.1017/S0263574721000229 Published online by Cambridge University Press

Table IV. Assumed values of unknown parameters and measurement noise ratio.

$u_{K[R]}$	u_E	u_G	$\|\delta\Delta E_{[model]}\|/\|\Delta E_{[model]}\|$
0.001rad	2×10^{-5}rad/Nm	0.0004 rad	$N\sim[0,(0.005/3)^2]$

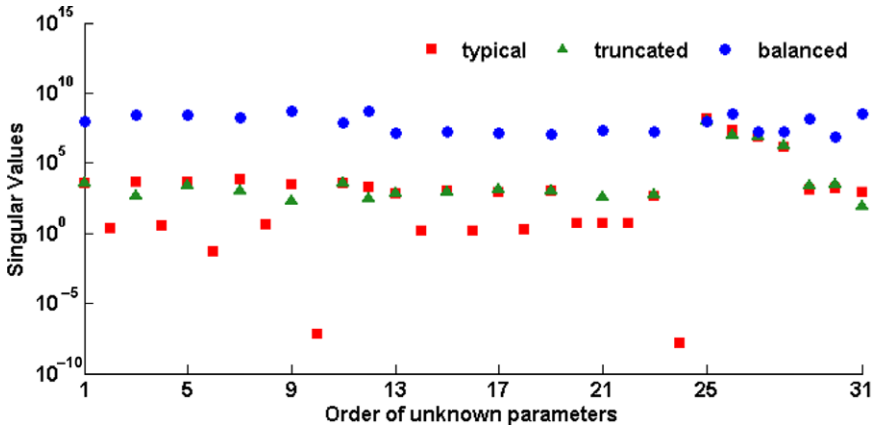


Fig. 6. Singular values of Jacobians in non-kinematic models.

5.2.3. Stability of the identification results. Now, we test whether the equalized (truncated and then balanced) singular values benefit the stability of the identification results under measurement noise. The measurement noise is mainly attributed to the errors of the measurement instrument (given that a Faro vantage laser tracker is adopted) and the repeatability errors of the robot. Their main specifications are given in Section 6.1. According to Section 4, the translational geometric errors are identified separately by using a non-model-based CPA method. Therefore, the stability of their identification results is not evaluated in this step. $u_{K[R]}$ denotes the rotational geometric parameters in u_K. $\|\delta\Delta E_{[model]}\|/\|\Delta E_{[model]}\|$ denotes the measurement noise ratio in the model-based calibration and used in the way of Eqs. (38)–(43). Each equation runs 1000 times according to the distribution of $\|\delta\Delta E_{[model]}\|/\|\Delta E_{[model]}\|$ given in Table IV. The assumed values of each kind of unknown parameters are also listed in Table IV.

$$\Delta u_K = J_K^{+}\Delta E_K\left(1+\frac{\delta\Delta E_{[model]}}{\Delta E_{[model]}}\right), \tag{38}$$

$$\Delta u_C = J_C^{+}\Delta E_C\left(1+\frac{\delta\Delta E_{[model]}}{\Delta E_{[model]}}\right), \tag{39}$$

$$\begin{cases}\Delta u_K^1 = [J_K^1]^{+}\Delta E_K^1\left(1+\dfrac{\delta\Delta E_{[model]}}{\Delta E_{[model]}}\right)\\ \Delta u_K^2 = [J_K^2]^{+}\Delta E_K^2\left(1+\dfrac{\delta\Delta E_{[model]}}{\Delta E_{[model]}}\right)\end{cases}, \tag{40}$$

$$\begin{cases}\Delta u_C^1 = [J_C^1]^{+}\Delta E_C^1\left(1+\dfrac{\delta\Delta E_{[model]}}{\Delta E_{[model]}}\right)\\ \Delta u_C^2 = [J_C^2]^{+}\Delta E_C^2\left(1+\dfrac{\delta\Delta E_{[model]}}{\Delta E_{[model]}}\right)\end{cases}, \tag{41}$$

$$\begin{cases}\Delta u_K^1 = B\left(AJ_K^{(1)}B\right)^{+}A\Delta E_K^1\left(1+\dfrac{\delta\Delta E_{[model]}}{\Delta E_{[model]}}\right)\\ \Delta u_K^2 = B\left(AJ_K^{(2)}B\right)^{+}A\Delta E_K^2\left(1+\dfrac{\delta\Delta E_{[model]}}{\Delta E_{[model]}}\right)\end{cases}, \tag{42}$$

https://doi.org/10.1017/S0263574721000229 Published online by Cambridge University Press

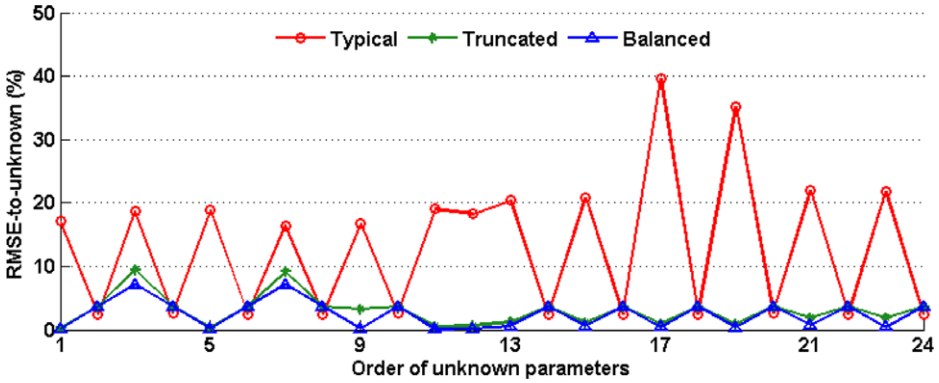


Fig. 7. Stability of the identification results of unknowns in kinematic models.

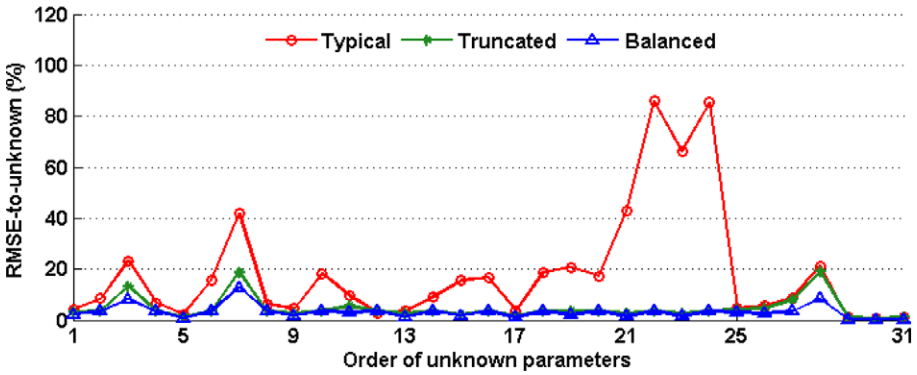


Fig. 8. Stability of the identification results of unknowns in non-kinematic models.

and

$$\begin{cases} \Delta u_C^1 = B\left(AJ_C^{(1)}B\right)^+ A\Delta E_C^1\left(1+\dfrac{\delta\Delta E_{[model]}}{\Delta E_{[model]}}\right) \\ \Delta u_C^2 = B\left(AJ_C^{(2)}B\right)^+ A\Delta E_C^2\left(1+\dfrac{\delta\Delta E_{[model]}}{\Delta E_{[model]}}\right) \end{cases} \tag{43}$$

Each element of $u_{K[R]}$, u_E and u_G is calculated 1000 times by using the corresponding identification models in Eqs. (38)–(43). Afterward, the root mean square error (RMSE) of each set of identified values (containing 1000 samples) and its proportion to the assumed value of corresponding unknown parameter can be calculated. The results are presented in Figs. 7 and 8. The reduced heights of the green and blue plots indicate that the new identification models improve the stability of the identification results of rotational parameters significantly. Meanwhile, the results about u_E and u_G are not too sensitive to the condition number of Jacobians and measurement noise. In sum, similar to the equalization for singular values as shown in Figs. 5 and 6, the stability of the results about rotational parameters ($u_{K[R]}$, u_E and u_G) shown in Figs. 7 and 8 are smoothed to relatively unified levels.

The stability of the identification results of translational geometric errors are also presented in Figs. 7 and 8. For typical identification models, the measurement noise ratio is $\|\delta\Delta E_{[model]}\|/\|\Delta E_{[model]}\|$ given in Table IV. For truncated and balanced identification models, the measurement noise $\|\delta\Delta E_{[CPA]}\|$ depends on the standard deviation of the center of a fitted circle, which is obtained from the circle points by using the CPA method. If a laser tracker with a measurement accuracy of ± 0.02 mm and a robot with a positioning repeatability of ± 0.02 mm is used, then the measurement error of these circle points is calculated as their combined uncertainty (0.0094 mm). In other words, if 1000 centers are adopted for each translational geometric error (assumed to be 0.05 mm) and if each of these centers is fitted from 15 circle points, then the RMSE-to-unknown ratio is calculated as 0.0018 mm/0.05 mm = 3.6%.

https://doi.org/10.1017/S0263574721000229 Published online by Cambridge University Press

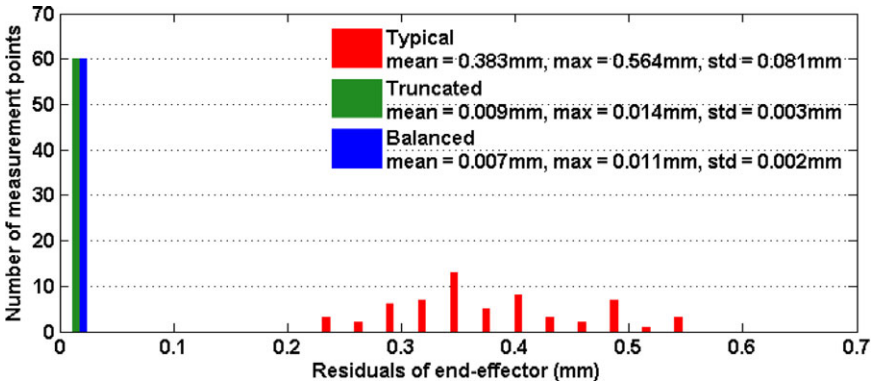


Fig. 9. Residuals after calibration by using kinematic models in the simulation.

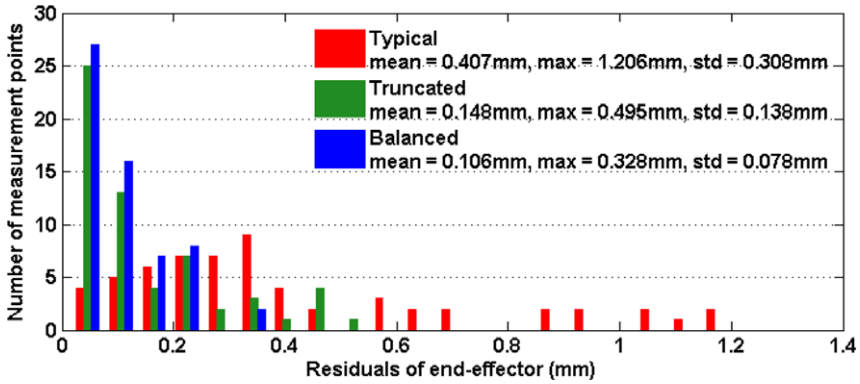


Fig. 10. Residuals after calibration by using non-kinematic models in the simulation.

5.2.4. Calibration accuracy. The last step is to test how much the positioning accuracy of the end effector can be improved by using the identification results with enhanced stability. The assumed values of unknowns and the measurement noise specified above are adopted. And three sets of 60 validation configurations (with an external payload of 6 kg) are randomly selected from the candidates generated in Section 5.1. The histograms of mean residuals after kinematic and non-kinematic calibrations are illustrated in Figs. 9 and 10, respectively. Results indicate that lower residuals can be acquired by using the truncated and balanced identification models. In addition, a comparison of Figs. 9 and 10 reveals that lower residuals are achieved by using the kinematic models than non-kinematic ones. This might be on the fact that the kinematic models consider less error sources (24 unknowns) than the non-kinematic ones do (31 unknowns). However, these simulation results do not confirm that kinematic calibrations are more accurate than non-kinematic ones in the real calibration because the importance of compliance parameters has been ignored by the kinematic models in the simulation.

6. Experiment

6.1. Experimental setup

A six-DOF BRTIRUS1510A robot with the nominal kinematic parameters given in Table I is adopted for the experiment. The repeatability after calibration is ±0.02 mm, the recommended maximum payload is 10 kg, and the arm length is 1.5 m. A Faro vantage laser tracker with the main specifications listed in Table V is also adopted. According to the effective working range of the laser tracker and robot arm, the measurement distance is constrained between 2 and 5 m. The counterweights (each is 0.5 kg and 16 mm thick) are located symmetrically around the Z_6-axis (as shown in the right part of Fig. 11) to minimize the eccentric influence of gravity centre on θ_6 because the compliance of joint 6 is not considered. The choices m_e = 0, 2, 4, 6 and 8 kg are available for the external payloads.

https://doi.org/10.1017/S0263574721000229 Published online by Cambridge University Press

Table V. Main specifications of the Faro vantage laser tracker.

Specifications	**Values**
Distance resolution	0.5 μm
Distance measurement accuracy	MPE: 16 μm + 0.8 μm/m
Angular measurement accuracy	MPE: 20 μm + 5 μm/m
Working range	0–80 m

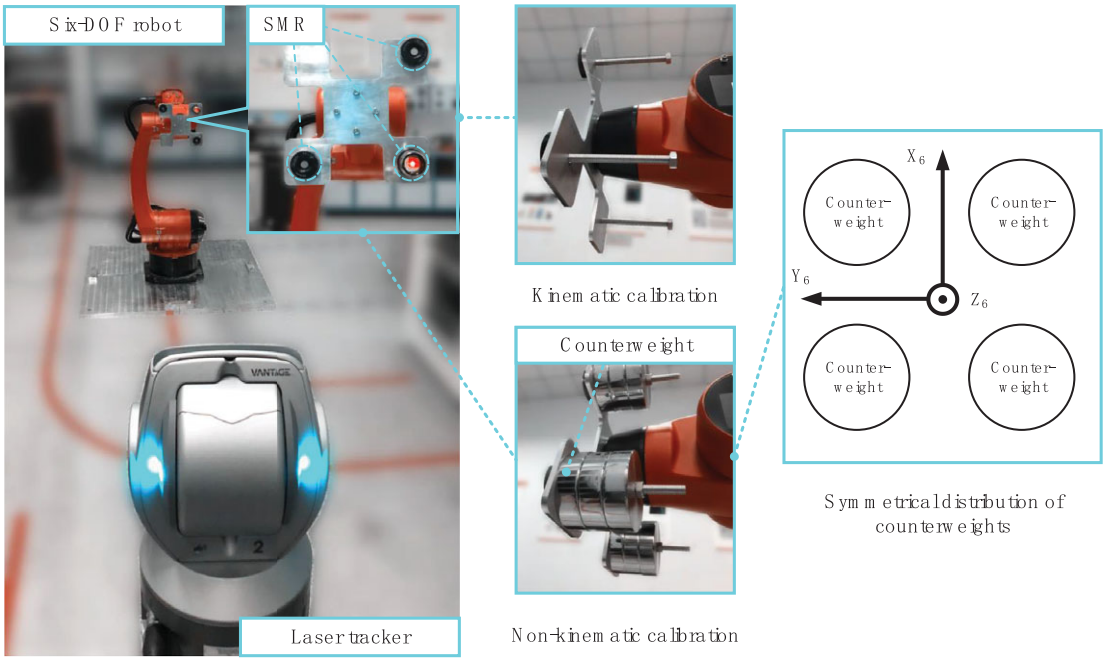


Fig. 11. Experimental setup.

The world frame F_{world}, base frame F_0, tool frame F_{tool}, and external payload frame F_e should be established before calibration.[6] Frames F_{world} and F_0 are defined by using the method proposed by Nubiola et al.[6] directly as shown in Fig. 12. Specifically, frame F_{world} is defined by using three positions of the SMR (spherically mounted reflector) near the base of robot. Then, the vectors of axis-1 (joint 1) and axis-2 (joint 2) in the frame F_{world} are acquired by using the CPA method. And frame F_0 is defined as one that moves 400 mm (d_1) from the origin of frame F_1 in –Z-direction. In this way, the geometric errors $\delta\alpha_1$, δa_1, $\delta\theta_1$, and δd_1 are removed. The real transformation from frame F_{world} to F_0 is also given in Fig. 12. F_{tool} is established by using the three positions of the SMR (as shown in Fig. 13 where vectors v_1 and v_2 are acquired from the three positions of the SMR, X_{tool}-axis is coincident with v_1, and Z_{tool}-axis is a cross product of v_1 and v_2) measured by the laser tracker with respect to frame F_6. Frame $F_6$is also defined according to ref. [6] as shown in Fig. 13 where the vectors of axis-5 and axis-6 in frame F_{world} are acquired by using the CPA method. Therefore, the unknown parameters $\delta\alpha_6$, δa_6, $\delta\theta_6$, and δd_6 are also eliminated from the identification models. The real transformation from frame F_6 to F_{tool} is given in Fig. 13. The real transformation (changing with the thickness of counterweights installed on the end effector) from frame F_6 to F_e is also given in Fig. 13.

6.2. Experimental procedures

The experimental procedures are illustrated in Fig. 14. Step 1 has already been done in the experimental setup (Section 6.1). Then, step 2 is to generate 46,656 and 933,120 candidate configurations for kinematic and non-kinematic calibrations, respectively. These configurations are the same with those in Section 5.1. Step 3 is to select the optimized measurement configurations (by using the

https://doi.org/10.1017/S0263574721000229 Published online by Cambridge University Press

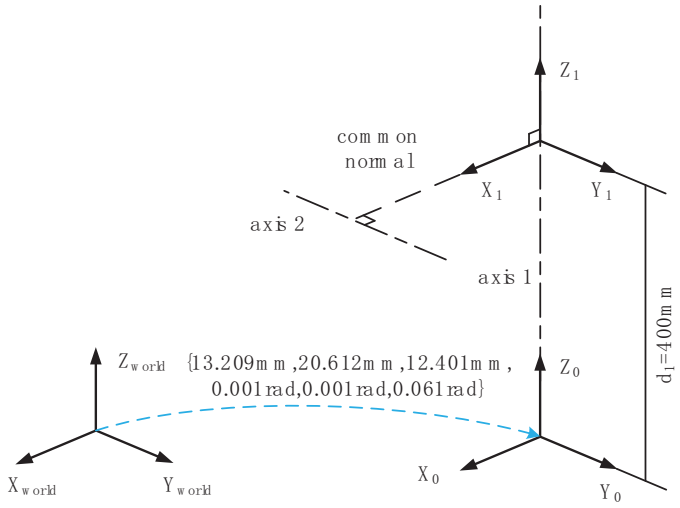


Fig. 12. Definitions of world frame F_{world} and base frame F_0.

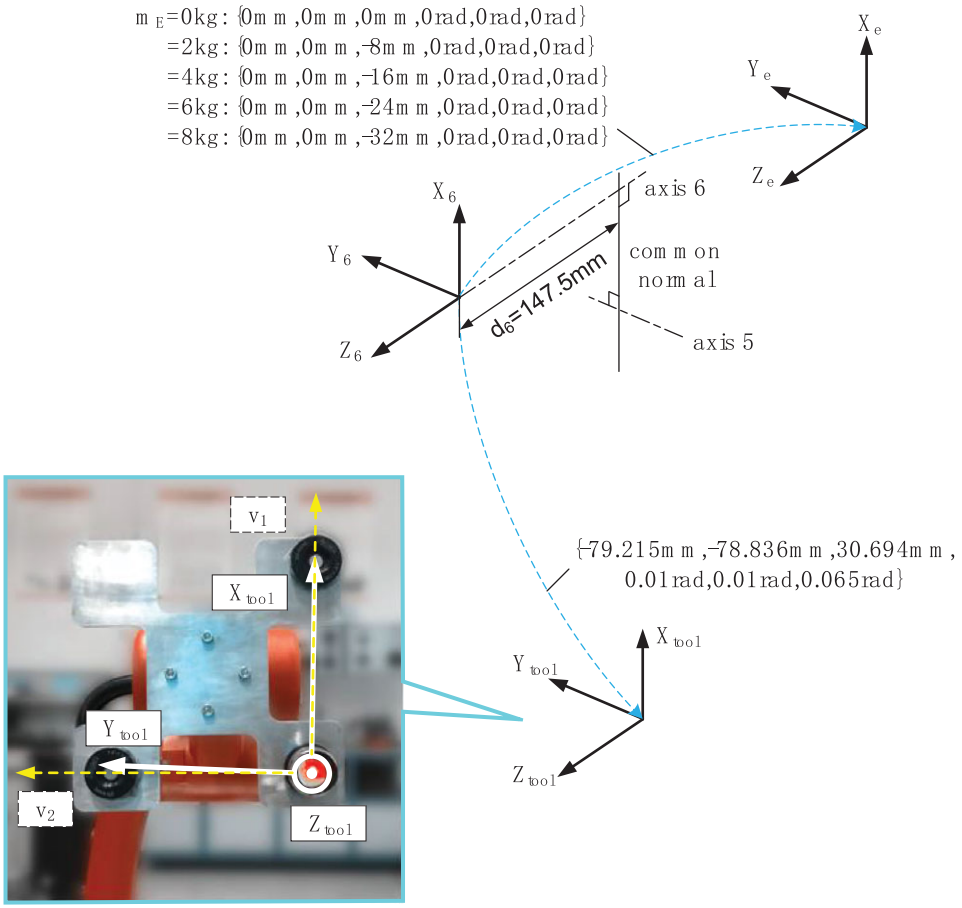


Fig. 13. Definitions of tool frame F_{tool}, joint 6 frame F_6, and external payload frame F_e.

DETMAX algorithm[28]) for each identification model and establish corresponding identification Jacobians accordingly, with consideration of the parameter elimination in Section 6.1. Then, the pose errors of frame F_{tool} are measured at these optimized configurations in step 4. Specifically, for the typical calibration method, all joints are involved to form the optimized configurations. Whereas

https://doi.org/10.1017/S0263574721000229 Published online by Cambridge University Press

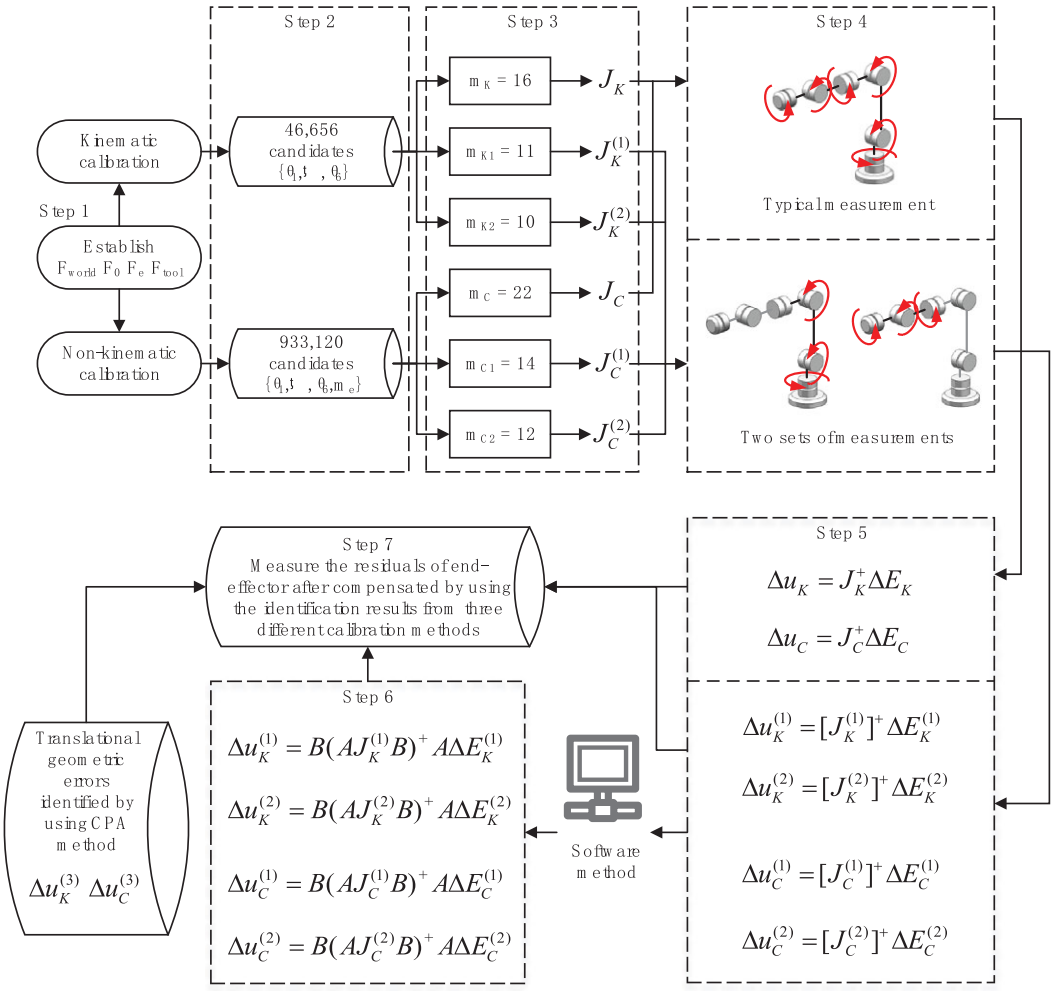


Fig. 14. Flowchart of the experimental procedure.

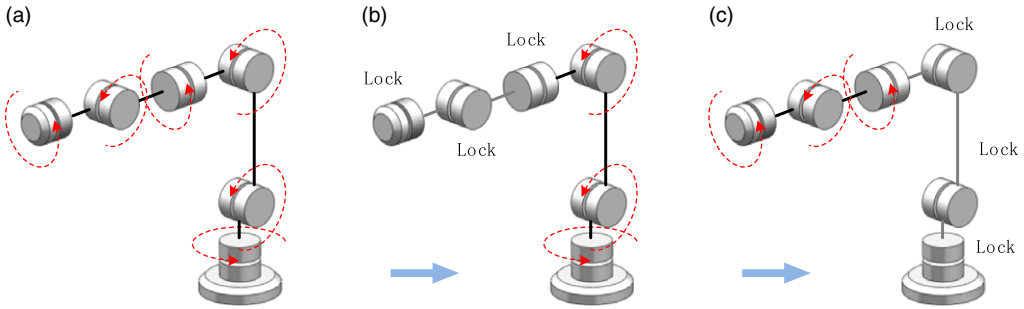


Fig. 15. Measurement configurations of the proposed calibration method. (a) CPA method to identify translational geometric errors. (b) Rotate first three joints to establish $\Delta E_*^{(1)} = J_*^{(1)} \Delta u_*^{(1)}$. (c) Rotate last three joints to establish $\Delta E_*^{(2)} = J_*^{(2)} \Delta u_*^{(2)}$.

for the proposed calibration method, first, the translational geometric errors are identified by using the CPA method as shown in Fig. 15(a). Then, as shown in Fig. 15(b), the pose errors of frame F_{tool} are measured at the optimized measurement configurations of joints 1–3, meanwhile, joints 4–6 are locked. In this way, the transformation from frame F_{tool} to F_3 is unchanged so that the pose errors of frame F_{tool} are independent with the unknown parameters of joints 4–6. Finally, the poses of F_{tool} are measured at the optimized measurement configurations of joints 4–6 as shown in Fig. 15(c) while joints 1–3 are locked. Therefore, frame F_3 is held with respect to frame F_1 to remove the impact of

https://doi.org/10.1017/S0263574721000229 Published online by Cambridge University Press

Table VI. Kinematic identification results acquired by using the typical, truncated and balanced identification models, respectively.

Unknown parameters	**Typical**	**Truncated**	**Balanced**
$\delta\alpha_2$ (rad)	0.0189	0.0196	0.0195
δa_2 (mm)	0.025	0.021	0.021
$\delta\theta_2$ (rad)	0.0071	0.0052	0.0054
δd_2 (mm)	−0.004	−0.003	−0.003
$\delta\alpha_3$ (rad)	−0.0112	−0.0098	−0.0094
δa_3 (mm)	0.024	0.018	0.018
$\delta\theta_3$ (rad)	0.0113	0.0090	0.0092
$\delta\beta_3$ (rad)	0.0024	0.0061	0.0061
$\delta\alpha_4$ (rad)	0.0087	0.0059	0.0060
δa_4 (mm)	0.007	0.008	0.008
$\delta\theta_4$ (rad)	0.0011	0.0015	0.0014
δd_4 (mm)	−0.023	−0.019	−0.019
$\delta\alpha_5$ (rad)	0.0066	0.0054	0.0052
δa_5 (mm)	−0.004	−0.006	−0.006
$\delta\theta_5$ (rad)	−0.0034	−0.0027	−0.0026
δd_5 (mm)	−0.008	−0.005	−0.005

unknown parameters of joints 1–3 on pose errors of F_{tool}. During the measurement, the laser beam might be blocked by the robot body and the supporter of SMR at some of the optimized measurement configurations due to the absence of SMR at the back of the supporter (more SMR bases are unavailable in our experiment). To solve this problem, these blocked configurations are modified slightly by just rotating one or two joints to make the three positions of SMR always visible from the laser tracker. And then the modified values of θ_1, θ_2, ..., and θ_6 are used to generate the identification Jacobians again to check whether the modified Jacobians are still well-conditioned.

In step 5, the Jacobians established in step 3 and the pose errors measured in step 4 are used to establish typical identification models (corresponding to Section 2) and the new submodels with truncated singular values (corresponding to Section 4.1). And in step 6, the submodels with truncated singular values are then improved to be the ones with balanced identification Jacobians (corresponding to Section 4.2) which are obtained by using the software method (on MATLAB). In step 5 and step 6, the rotational unknown parameters ($u_{K[R]}$, u_E and u_G) are eventually identified. Then in step 7, to compare the effectiveness of the different identification models, three sets of 60 randomly selected validation configurations (with an external payload of 6kg) that differ from those used in step 4 are used to measure the residuals of F_{tool} after compensation.

6.3. Experimental results and discussion

The kinematic and non-kinematic identification results are listed in Tables VI and VII, respectively. The mean residuals at each measurement point in the three sets of configurations (acquired by step 7) after the kinematic and non-kinematic calibrations are given in Figs. 16 and 17, respectively. The green plots indicate that the lower residuals can be acquired by using the identification models with truncated singular values (Section 4.1), and the blue plots prove that the residuals are further reduced by using the identification submodels with balanced Jacobians (Section 4.2). From the statistics (in the form of box plots) of these residuals as shown in Figs. 18 and 19, 38–46%, and 65–66% reductions of the mean residuals after using the truncated and balanced submodels, respectively, can be observed. Moreover, the mean residuals with the balanced submodels are reduced by 34–45% compared with the truncated ones. The improvements in these residuals from truncated to balanced submodels in the non-kinematic calibration are not too significant (34%). However, given that the balanced Jacobians are only generated by using the software method without additional costs after completing the measurement configurations for the truncated submodels, this attempt is still deemed valuable for improving identification accuracy.

https://doi.org/10.1017/S0263574721000229 Published online by Cambridge University Press

Table VII. Non-kinematic identification results acquired by using the typical, truncated and balanced identification models, respectively.

Unknown parameters	**Typical**	**Truncated**	**Balanced**
$\delta\alpha_2$ (rad)	0.0112	0.0114	0.0114
δa_2 (mm)	0.024	0.021	0.021
$\delta\theta_2$ (rad)	0.0064	0.0051	0.0051
δd_2 (mm)	−0.003	−0.003	−0.003
$\delta\alpha_3$ (rad)	−0.0081	−0.0076	−0.0075
δa_3 (mm)	0.023	0.018	0.018
$\delta\theta_3$ (rad)	0.0092	0.0096	0.0096
$\delta\beta_3$ (rad)	0.0052	0.0049	0.0051
$\delta\alpha_4$ (rad)	0.0053	0.0048	0.0047
δa_4 (mm)	0.005	0.008	0.008
$\delta\theta_4$ (rad)	0.0012	0.0010	0.0011
δd_4 (mm)	−0.014	−0.019	−0.019
$\delta\alpha_5$ (rad)	0.0032	0.0030	0.0033
δa_5 (mm)	−0.009	−0.006	−0.006
$\delta\theta_5$ (rad)	−0.0031	−0.0028	−0.0028
δd_5 (mm)	−0.003	−0.006	−0.006
λ_2 (rad/Nm)	1.65×10^{-7}	1.39×10^{-7}	1.32×10^{-7}
λ_3 (rad/Nm)	3.83×10^{-6}	3.51×10^{-6}	3.37×10^{-6}
λ_4 (rad/Nm)	4.58×10^{-5}	4.30×10^{-5}	4.17×10^{-5}
λ_5 (rad/Nm)	1.09×10^{-5}	1.09×10^{-5}	1.10×10^{-5}
ξ_1 (rad)	0.0003	0.0002	0.0002
ξ_2 (rad)	0.0003	0.0006	0.0007
ξ_3 (rad)	0.0005	0.0007	0.0009

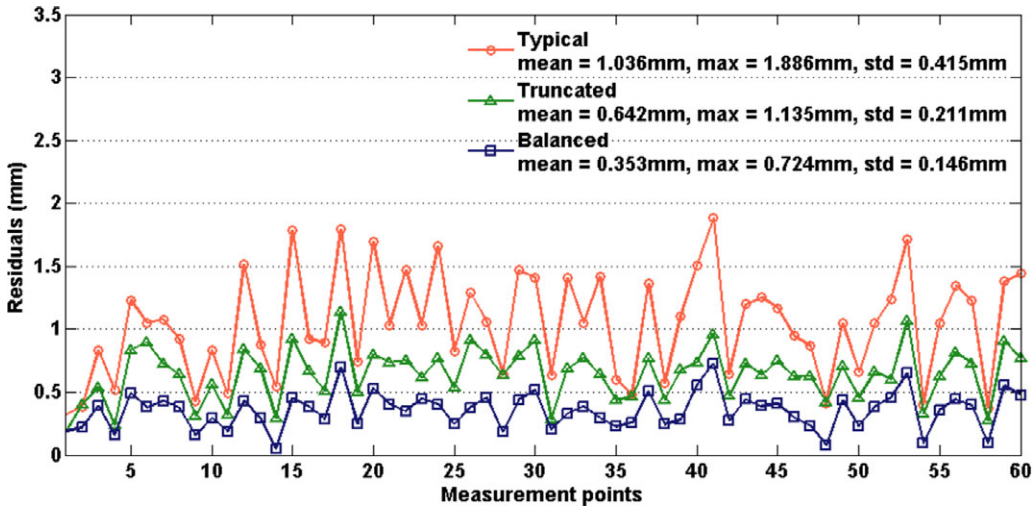


Fig. 16. Residuals after calibration by using different kinematic identification models.

Besides, the residuals after the non-kinematic calibration (Fig. 19) are lower than those after the kinematic calibration (Fig. 18). The differences from the simulation results may demonstrate the inference presented at the end of Section 5, that is, the non-kinematic calibration with an additional consideration of compliance parameters might be more accurate, especially in the case where the identification models are improved to be well-conditioned (with equalized singular values).

https://doi.org/10.1017/S0263574721000229 Published online by Cambridge University Press

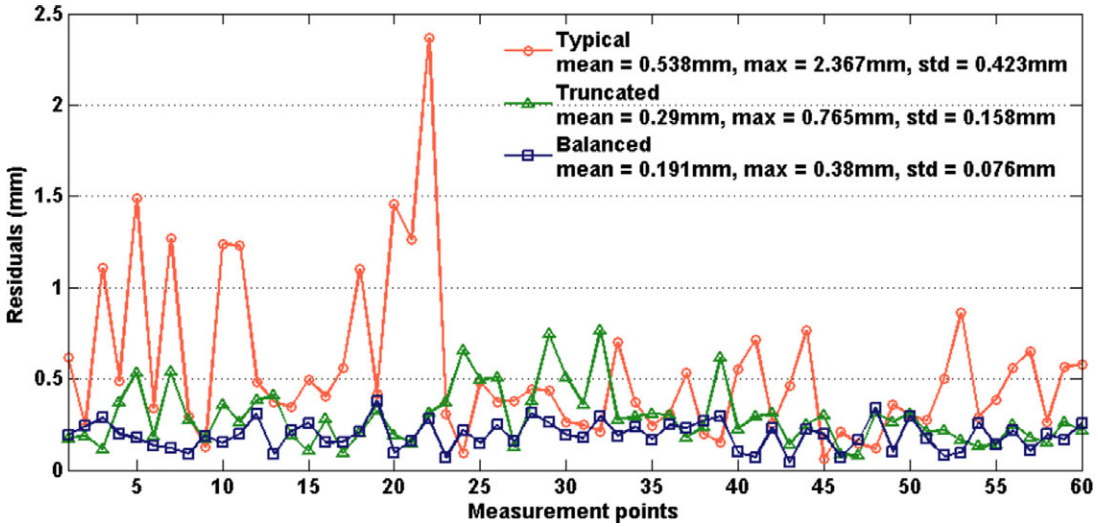


Fig. 17. Residuals after calibration by using different non-kinematic identification models.

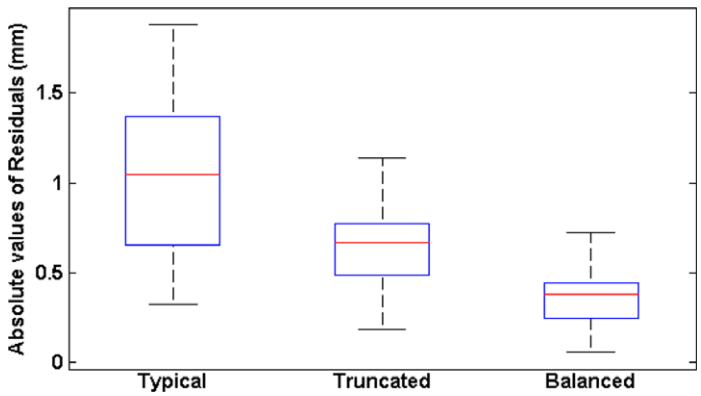


Fig. 18. Statistics of residuals by using different kinematic identification models.

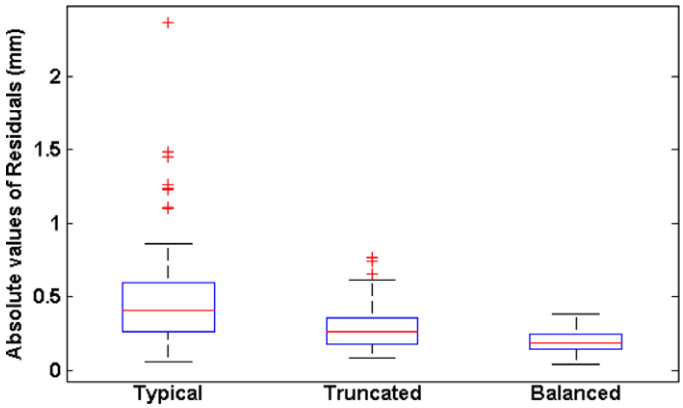


Fig. 19. Statistics of residuals by using different non-kinematic identification models.

7. Conclusion

The condition number and observability index of identification Jacobians are improved by using the proposed two-step equalization method for singular values. The comparison results from the simulation indicate that the stability and identifiability of the results can be improved by using the submodels

https://doi.org/10.1017/S0263574721000229 Published online by Cambridge University Press

with equalized singular values. Experimental results also verify the effectiveness of the new identification submodels in a real calibration performed on a six-DOF robot by testing the residuals. The experimental setup for this method is the same as that for the typical laser method without requiring additional sensors, measurement instruments, or auxiliary equipment. The only cost for this method is that three sets of measurement configurations are required for three groups of unknowns, which may extend the calibration time.

The matrix balance method introduced in this study centralizes the singular values of truncated submodels into smaller ranges but does not equalize them exactly, especially in the non-kinematic identification model for joints 1–3 (the improved condition number is 77.6). Some other algorithms might be highly capable of narrowing the gaps between singular values. In this case, the identification accuracy can be further improved by using better-conditioned submodels. This issue will be considered in our future work.

Acknowledgement

Funding: This work was supported by the Young Scientists Fund of National Natural Science Foundation of China [grant number 51805039]; the General Project of Science and Technology Plan of Beijing Municipal Education Commission [grant number KM201911232024]; the Supplementary and Supportive Project for Teachers at Beijing Information Science & Technology University (2018-2020) [grant number 5029011103].

Conflict of Interest

The authors declare none.

References

1. A. Y. Elatta, P. G. Li, L. Z. Fan and D. Yu, "An overview of robot calibration," *Inf. Technol. J.* **3**(1), 74–78 (2004).
2. C. Gang, L. Tong, C. Ming, J. Q. Xuan and S. H. Xu, "Review on kinematics calibration technology of serial robots," *Int. J. Precision Eng. Manuf.* **15**(8), 1759–1774 (2014). https://doi.org/10.1007/s12541-014-0528-1.
3. L. Ma, P. Bazzoli and P. M. Sammons, "Modeling and calibration of high-order joint-dependent kinematic errors for industrial robots," *Rob. Comput. Integr. Manuf.* **50**, 153–167 (2018). https://doi.org/10.1016/j.rcim.2017.09.006.
4. C. H. Gong, J. X. Yuan and J. Ni, "Nongeometric error identification and compensation for robotic system by inverse calibration," *Int. J. Mach. Tools Manuf.* **40**(14), 2119–2137 (2000). https://doi.org/10.1016/s0890-69550000023-7.
5. Z. Roth, B. Mooring and B. Ravani, "An overview of robot calibration," *IEEE J. Rob. Autom.* **3**(5), 377–385 (1987). https://doi.org/10.1109/jra.1987.1087124.
6. A. Nubiola and I. A. Bonev, "Absolute calibration of an ABB IRB 1600 robot using a laser tracker," *Rob. Comput. Integr. Manuf.* **29**(1), 236–245 (2013). https://doi.org/10.1016/j.rcim.2012.06.004.
7. Y. Wu, A. Klimchik, S. Caro, B. Furet and A. Pashkevich, "Geometric calibration of industrial robots using enhanced partial pose measurements and design of experiments," *Rob. Comput. Integr. Manuf.* **35**, 151–168 (2015). https://doi.org/10.1016/j.rcim.2015.03.007.
8. C. Li, Y. Q. Wu and H. Lowe, "POE-based robot kinematic calibration using axis configuration space and the adjoint error model," *IEEE Trans. Rob.* **32**(5), 1264–1279 (2016). https://doi.org/10.1109/tro.2016.2593042.
9. G. B. Gao, G. Q. Sun, J. Na, Y. Guo and X. Wu, "Structural parameter identification for 6 DOF industrial robots," *Mech. Syst. Signal Process.* (2017). https://doi.org/10.1016/j.ymssp.2017.08.011.
10. X. Y. Chen, Q. J. Zhang and Y. L. Sun, "Non-kinematic calibration of industrial robots using a rigid-flexible coupling error model and a full pose measurement method," *Rob. Comput. Integr. Manuf.* **57**, 46–58 (2019). https://doi.org/10.1016/j.rcim.2018.07.002.
11. Y. Qiao, Y. P. Chen and B. Chen, "A novel calibration method for multi-robots system utilizing calibration model without nominal kinematic parameters," *Precision Eng.* **50**, 211–221 (2017). https://doi.org/10.1016/j.precisioneng.2017.05.009.
12. A. Nubiola and I. A. Bonev, "Absolute robot calibration with a single telescoping ballbar," *Precision Eng.* **38**(3), 472–480 (2014). https://doi.org/10.1016/j.precisioneng.2014.01.001.
13. A. Nubiola and I. A. Bonev, "Non-kinematic calibration of a six-axis serial robot using planar constraints," *Precision Eng.* **40**(3), 472–480 (2015). https://doi.org/10.1016/j.precisioneng.2014.12.002.
14. Y. Y. Cai, H. Gu, C. Li and H. S. Liu, "Easy industrial robot cell coordinates calibration with touch panel," *Rob. Comput. Integr. Manuf.* **50**, 276–285 (2018). https://doi.org/10.1016/j.rcim.2017.10.004.
15. W. Wang, F. Liu and C. Yun, "Calibration method of robot base frame using unit quaternion form," *Precision Eng.* **41**, 47–54 (2015). https://doi.org/10.1016/j.precisioneng.2015.01.005.

https://doi.org/10.1017/S0263574721000229 Published online by Cambridge University Press

16. S. S. Radhe, S. Santosh, B. Laxmidhar and K. S. Venkatesh, "Position-based visual servoing of a mobile robot with an automatic extrinsic calibration scheme," *Robotica* **38**(5), 831–844 (2020). https://doi.org/10.1017/S0263574719001115.
17. J. H. Borm and C. H. Menq, "Determination of optimal measurement configurations for robot calibration based on observability measure," *Int. J. Rob. Res.* **10**(1), 51–63 (1991). https://doi.org/10.1177/027836499101000106.
18. Z. T. Fu, J. S. Dai, K. Yang, X. B. Chen and P. López-Custodio, "Analysis of unified error model and simulated parameters calibration for robotic machining based on Lie theory," *Rob. Comput. Integr. Manuf.* **61**, 1–14 (2020). https://doi.org/10.1016/j.rcim.2019.101855.
19. A. Joubair, A. S. Tahan and I. A. Bonev, "Performances of Observability Indices for Industrial Robot Calibration," *IEEE/RSJ International Conference on Intelligent Robots and Systems (IROS)* (2016) pp. 2477–2484. https://doi.org/10.1109/iros.2016.7759386.
20. S. Elie and N. Shadi, "Kinematic calibration of serial manipulators using Bayesian inference," *Robotica* **36**(5), 738–766 (2018). https://doi.org/10.1017/S0263574718000024.
21. C. Genliang, K. Lingyu, L. Qinchuan and W. Hao, A simple two-step geometric approach for the kinematic calibration of the 3-PRS parallel manipulator," *Robotica*. **37**(5), 837–850 (2019). https://doi.org/10.1017/S0263574718001352.
22. C. Chenguang, L. Jinguo, N. Zhiyu and Q. Ruolong, "An improved kinematic calibration method for serial manipulators based on POE formula," *Robotica* **36**(8), 1244–1262 (2018). https://doi.org/10.1017/S0263574718000280.
23. A. Klimchik, B. Furet, S. Caro and A. Pashkevich "Identification of the manipulator stiffness model parameters inindustrial environment," *Mech. Mach. Theory* **90**, 1–22 (2015). https://doi.org/10.1016/j.mechmachtheory.2015.03.002.
24. K. Kamali and I. A. Bonev, "Optimal experiment design for elasto-geometrical calibration of industrial robots," *IEEE/ASME Trans. Mechatron.* **24**(6), 2733–2744 (2019). https://doi.org/10.1109/tmech.2019.2944428.
25. N. A. Theissen, T. Laspas and A. Archenti, "Closed-force-loop elastostatic calibration of serial articulated robots," *Rob. Comput. Integr. Manuf.* **57**, 86–91 (2019). https://doi.org/10.1016/j.rcim.2018.07.007.
26. T. Huang, D. Zhao, F. W. Yin, W. J. Tian and D. G. Chetwynd, "Kinematic calibration of a 6-DOF hybrid robot by considering multicollinearity in the identification Jacobian," *Mech. Mach. Theory* **131**, 371–384 (2019). https://doi.org/10.1016/j.mechmachtheory.2018.10.008.
27. A. Nahvi and J. M. Hollerbach, "The Noise Amplification Index for Optimal Pose Selection in Robot Calibration," *1996 IEEE International Conference on Robotics and Automation*, vol. 1(1) (1996) pp. 647–654. https://doi.org/10.1109/robot.1996.503848.
28. T. J. Mitchell, "An algorithm for the construction of 'D-Optimal' experimental designs," *Technometrics* **42**(1), 48–54 (2000). https://doi.org/10.1080/00401706.2000.10485978.
29. M. E. Sklar, "Geometric Calibration of Industrial Manipulators by Circle Point Analysis," *Proceedings of the 2nd Conference on Recent Advances in Robotics* (1989) pp. 178–202.
30. J. Santolaria, J. Conte, M. Pueo and C. Javierre, "Rotation error modeling and identification for robot kinematic calibration by circle point method," *Metrol. Meas. Syst.* **21**(1), 85–98 (2014). https://doi.org/10.2478/mms-2014-0009.
31. Y. S. Cho, H. M. Do and J. N. Cheong, "Screw based kinematic calibration method for robot manipulators with joint compliance using circular point analysis," *Rob. Comput. Integr. Manuf.* (2018). https://doi.org/10.1016/j.rcim.2018.08.001.

https://doi.org/10.1017/S0263574721000229 Published online by Cambridge University Press